photonics

MDPI

Letter

The Significance of Carrier Leakage for Stable Lasing in Split-Well Direct Phonon Terahertz Quantum Cascade Lasers

Nathalie Lander Gower, Silvia Piperno and Asaf Albo *

Faculty of Engineering, Bar-Ilan University, Ramat Gan 5290002, Israel; nathilander@gmail.com (N.L.G.); silvia.piperno@biu.ac.il (S.P.)

* Correspondence: asafalbo@gmail.com

Received: 24 June 2020; Accepted: 12 August 2020; Published: 14 August 2020

Abstract: We studied the temperature performance of split-well direct phonon terahertz quantum cascade lasers and found that it is limited by a lasing instability that becomes significant as the temperature increases. When the hot electrons of the upper laser level cannot scatter effectively to excited states due to the high radiative barriers of the structures, a lasing instability occurs, which limits the temperature performance.

Keywords: THz-QCLs; carrier leakage; lasing instability

1. Introduction

The maximum operating temperature (T_{max}) reported so far for terahertz-quantum cascade lasers (THz-QCLs) is ~210 K [1]. For THz-QCLs based on spatially vertical transitions, the major physical mechanism that limits T_{max} was identified as thermally activated LO-phonon scattering from the upper to the lower laser level [2]. A strategy for counteracting the temperature degradation of THz-QCLs is to reduce the thermally activated LO-phonon scattering by using diagonal structures [3]. In previous studies, we investigated potential mechanisms that limit the temperature performance of diagonal THz-QCLs and identified that thermally activated leakage of charge carriers into the continuum [4] or into excited bound states [5,6] reduces the upper laser level lifetime. Structures with widely separated higher-laying excited states enabled by using high barriers were implemented to reduce the adverse effects of these mechanisms. The suppression of those leakage channels in a resonant-phonon [5] and two-well [7] schemes was demonstrated—as indicated by the observation of negative differential resistance (NDR) at room temperature. To improve the temperature performance of these lasers, a new THz-QCL structure, named split-well direct phonon (SWDP), has been suggested as an ideal platform for studying the carrier dynamics [8]. As a result of this scheme, the lasers benefit from flexible design and the efficient isolation of laser levels from excited and continuum states [4–6]. A clean three-level system, in which most of the electrons reside in the three lowest subbands even at elevated temperatures, is achieved in the SWDP design, as indicated by the NDR behavior at room temperature. Due to the enhanced flexibility in the design, these schemes serve as a good platform for studying the mechanisms that govern the temperature degradation. Here, we studied different realizations of the SWDP scheme using different barrier compositions than the original contribution and analyzed their performance. We found that the lasers are limited by a lasing instability [9,10] that becomes significant as the temperature increases.

In this paper, diagonal [3], (f ~0.22) SWDP THz-QCLs with $Al_{0.30}Ga_{0.70}As$ potential barriers and carrier density per cascade of ~3×10^{10} cm^{-2}, (Figure 1) are investigated. The molecular beam epitaxy (MBE) wafer is labeled VB0843. The device is called Device 1 for simplicity. Further information about this design is presented in Tables 1 and 2.

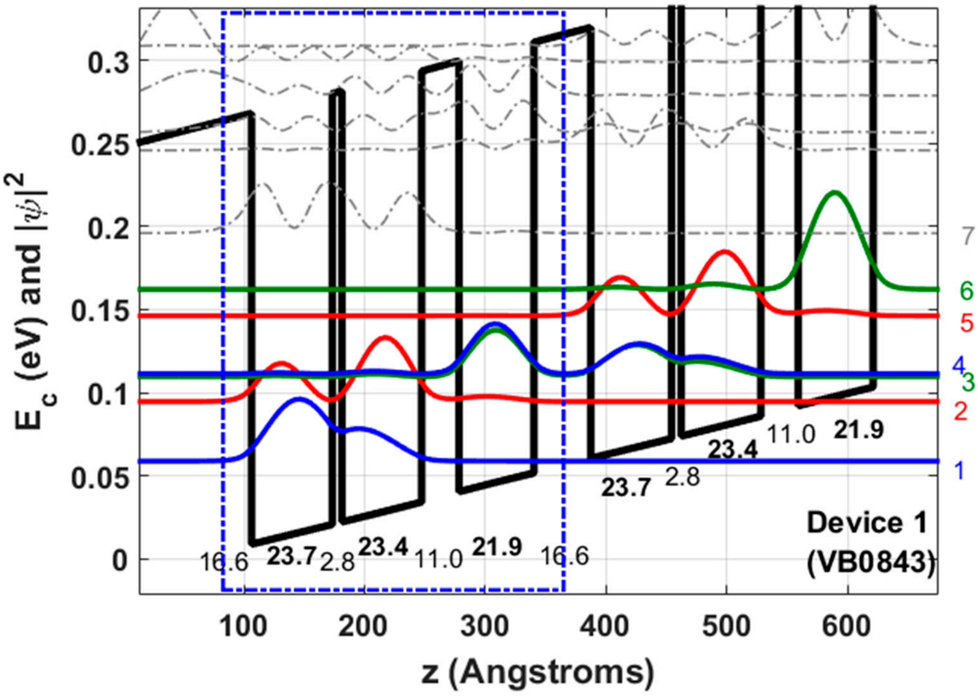

Figure 1. Band diagram of two sequential periods labeled *module i* (left, the dashed-dotted box) and *module i+1* (right) of Device 1 (wafer VB0843). In the figure there are various distortions of the wave functions (different shape and amplitude of wavefunctions for the same levels) due to the presentation of only two periods. The two periods are preferred by us due to presentation considerations.

In Figure 1, a structure with three fundamental subbands in each module is shown. All other levels seen in the figure are considered parasitic. A direct-phonon scattering scheme is formed by aligning the upper laser level (ULL, level 3 in the scheme) and the injector level (level 4 in the scheme), a scheme that resembles the one of a two-well (TW) structure [11–13]. Direct-phonon structures proved to be superior to resonant-phonon (RP) ones, hence the motivation to keep this design for SWDP. One of the main advantages of the scheme is the very fast depopulation of the lower laser level (LLL), reached by longitudinal-optical (LO)-phonon scattering only, with no resonance coupling involved in the process. Furthermore, its sensitiveness to misalignment of the laser levels (due to the Poisson effect that causes band bending [7,14,15]) is lower. Another advantage is that the added barrier of the SWDP reduces carrier leakage channels to a larger extent, including intermodule leakage.

The energy splitting between levels 1 and 2 (see Figure 1) is controlled by using an intra-well thin barrier. The energy gap can be changed to be the exact LO-phonon energy (E_{21} = 36 meV) by adjusting the thickness of the intra-well barrier. Reaching this exact energy level enables the fastest LO-phonon scattering rate depopulating the LLL. Additionally, in the SWDP design, the resonant LO-phonon scattering condition of E_{21} = 36 meV is kept even when pushing the excited levels to higher energies, thanks to the thickness adjustability of the intra-well barrier [8]. It is essential to keep the fastest possible LLL depopulation rate, as demonstrated by several works that establish the disadvantages of slow LLL depopulation on the laser performance for THz-QCLs [5,7,16–18]. Nevertheless, high laser performance can also be achieved with E_{21} > 36 meV [19,20].

2. Discussion

The maximum temperature reached in Device 1 (fabricated from wafer VB0843) was of about 120 K. In Figure 1, we can appreciate the fact that the excited states (levels ≥ 7) are well separated from the three active subbands (levels 1–3) [8]. We can see that the first excited state (level 7) is not only located ~85 meV above the ULL, but it is also spatially located in the next neighboring quantum well. As the scheme in Figure 1 indicates, this excited state and the ULL hardly overlap. Moreover, the ULL of the second module (level 6) in the higher energy side of the scheme (*module i+1*), is also energetically positioned bellow the first excited state (level 7). We infer from these facts that there is a decrease of intermodule leakage as compared to TW structures [7]. The lasing frequency observed was of ~4.02 THz (~17 meV, Figure 2 inset and Table 2) in comparison to the designed lasing value of ~3.60 THz (Table 1).

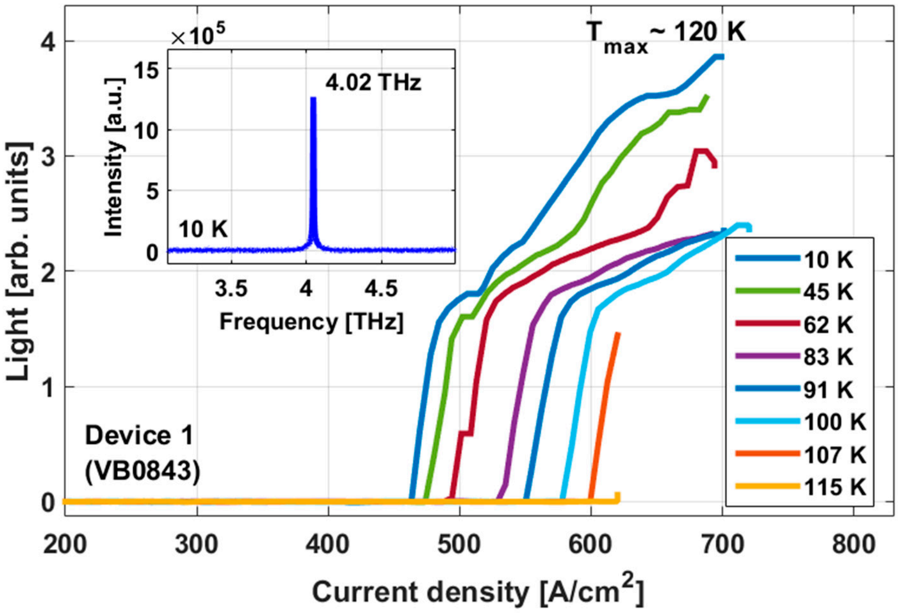

Figure 2. Pulsed light–current and spectrum (inset) measurements of Device 1 (wafer VB0843). The measurements were conducted in pulsed mode with square pulse form at the width of 500 ns and frequency of 500 Hz.

The L–I curves of Device 1 in Figure 2 show a two-slope behavior of the power output (P_{out}). According to the energy schemes in Figure 1, the second reduced slope cannot be explained by intermodule leakage. An alternative explanation for the slope reduction might be the heating of the ULL electrons upon lasing [21–23]. Furthermore, the I–V curves in Figure 3 demonstrate that the device has NDR at room temperature. This is indication for an effective isolation of the three active laser states from the excited and continuum states, i.e., a clean three laser-level system was obtained in this device. At temperatures close to T_{max}, we observe fluctuations in the I–V curves (Figure 3) indicating lasing instability [9,24]. The occurrence of fluctuations in the I–V curves is correlated with the disappearance of the second slope from the L–I curves in the vicinity of T_{max} and to fast deterioration of the laser intensity (Figure 2).

Table 1. Main nominal design parameters and device data.

Device	Lasing Energy [meV]	E_{21} [meV]	Oscillator Strength	Nom. Expected Activation Energy [meV]	E_{47} [meV]	Layer Sequence [#ML*], Barrier Composition and Doping Level	Process Details
Device 1 (VB0843), (Figure 1)	14.9	36	0.22	21.1	84.6	**16.6**/<u>*23.7*</u>/**2.8**/<u>*23.4*</u>/**11.0**/*21.9* 355 periods *GaAs*/**$Al_{0.30}Ga_{0.70}As$** 2.24×10^{16} cm^{-3} in the 23.7 and 23.4 ML wells (2.98×10^{10} cm^{-2}).	Metal–metal (100 Å Ta/2500 Å) Top contact n^+ layer was removed Dry etched Mesa size 150 µm × 1.8 mm
Device 2 (VB0837) ([8])	11.1	34.5	0.26	24.9	72.5	**9.0**/<u>*24.8*</u>/**3.5**/<u>*24.8*</u>/**17.3**/*24.8* 353 periods *GaAs*/mixed barriers **$Al_{0.55}Ga_{0.45}As$ (Injector) and $Al_{0.15}Ga_{0.85}As$ (Radiative, Intrawell)** 2.13×10^{16} cm^{-3} in the 24.8 ML wells (2.98×10^{10} cm^{-2}).	Metal-metal (100 Å Ta/2500 Å Au) Top contact n^+ layer was removed Dry etched Mesa size 150 µm × 1.8 mm
Device 3 (VB0847) (Figure 5)	10.7	34.5	0.25	25.3	75.1	**9.0**/<u>*26.2*</u>/**3.5**/<u>*25.8*</u>/**10.3**/*26.9* 362 periods *GaAs*/mixed barriers: **$Al_{0.55}Ga_{0.45}As$ (Injector), $Al_{0.30}Ga_{0.70}As$ (Radiative) and $Al_{0.15}Ga_{0.85}As$ (Intrawell)** 2.03×10^{16} cm^{-3} in the 26.2 and 25.8 ML wells (2.98×10^{10} cm^{-2}).	Metal-metal (100 Å Ta/2500 Å) Top contact n^+ layer was removed Dry etched Mesa size 150 µm × 1.8 mm

* #ML is the number of monolayers, **AlGaAs** barriers are in **bold** and *GaAs* wells are *italicized*. the barriers' composition and doping data are given in detail, the doped layer in the sequence is underscored.

Table 2. Device parameters and performance.

Device	Injection Coupling $(2\hbar\Omega_{ij})$ [meV]	Design Electric Field [kV/cm]	$\tau^0{}_{ul}$ [ps] *	$\tau^0{}_{21}$ [ps] **	IFR Gain Broadening [meV] ***	Exp. Lasing Energy [meV]	Expected Activation Energy [meV]	J_{th} (10 K) [A/cm^2]	J_{max} (10 K)[A/cm^2]	Dynamic Range (10 K) [A/cm^2]	J_{max} (290 K) [A/cm^2]	T_{max} [K]
Device 1 (VB0843), (Figure 1)	1.87	18.4	1.23	0.17	4.19	16.6	19.4	463	708	245	657	120
Device 2 (VB0837) ([8])	2.08	16.5	1.21	0.18	4.37	10.05	25.5	578	928	350	750	170
Device 3 (VB0847) (Figure 5)	2.12	16.8	1.08	0.19	4.10	10.8	25.2	578	625	47	646	57

* ULL to LLL raw LO-phonon scattering time. ** LLL (level 2) to Injector (level 1) LO–phonon scattering time. *** Calculated according to Flores and Albo [25].

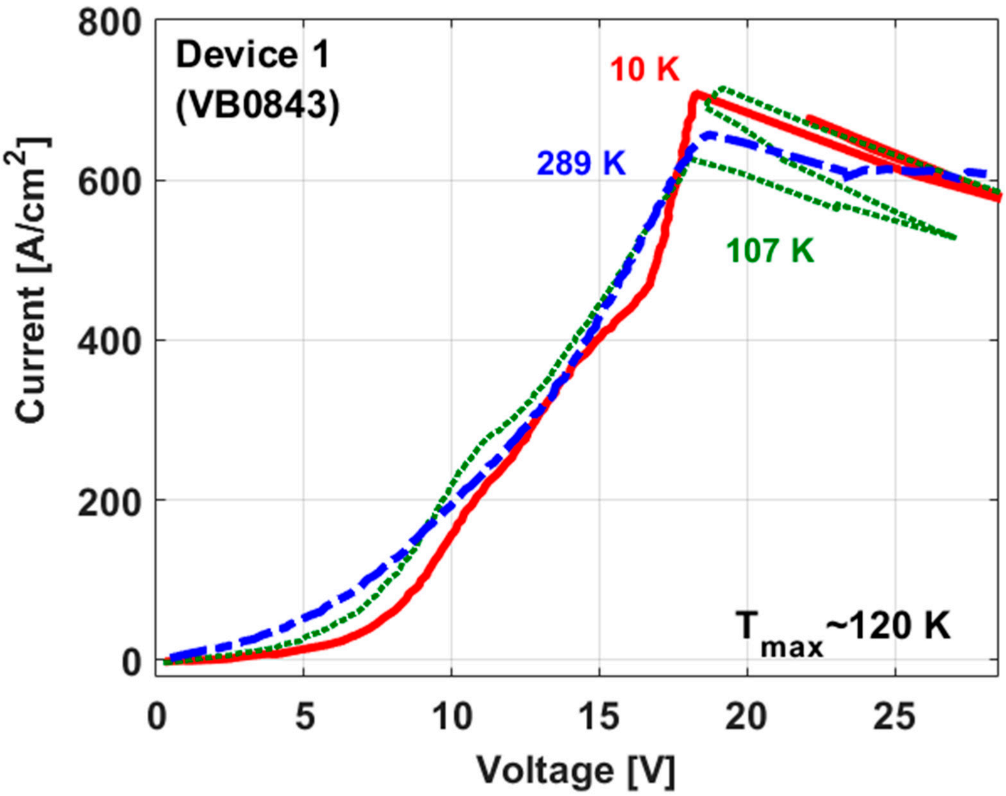

Figure 3. Current curves as a function of voltage for Device 1 (wafer VB0843) at low, maximum, and room temperatures. The measured maximum operating (lasing) temperature is 120 K, as indicated.

The laser instability behavior is indicated by the faster drop in power versus temperature as observed in the L–I curves in Figure 2 and the fluctuations in the I–V curves in Figure 3 that become very significant as the temperature approaches T_{max}. In fact, it seems that the temperature performance as indicated by T_{max} is limited by the lasing instability rather than the population inversion drop.

The change in light (P_{out}) as a function of temperature was analyzed. Arrhenius plots according to Albo and Hu's method [2] using $\ln\left(1 - \frac{P_{out}(T)}{P_{out\,max}}\right) \approx \ln(a) - \frac{E_a}{kT}$ (where a is a constant), were used to extract the activation energies (E_a). Data close to T_{max} was ignored, and reasonable activation energy values were obtained for Device 1 (Figure 4). Our procedure is validated, as can be seen, by the smooth curves in the temperature range used for extraction. The dependence on temperature of the current dynamic range $\Delta J_d = (J_{max} - J_{th})$ was also analyzed, implying the dependence of the output lasing power on temperature. The best fit to the data using Arrhenius plots according to $\ln\left(1 - \frac{\Delta J_d(T)}{\Delta J_{d\,max}}\right) \approx \ln(b) - \frac{E_a}{kT}$, where b is a constant, was utilized to extract the activation energies for the current dynamic range, as done before for P_{out}. No contribution from parallel leakage current exists, leading to the fact that the maximum current J_{max} results only from the transport through the active laser states. Thus, the use of the dynamic range for the analysis was reasonable. Therefore, the stimulated emission rate and generated radiation power, with much lower data fluctuations, are directly reflected by the dynamic range. The main assumption is that $\Delta J_d = (J_{max} - J_{th}) \approx (J_{max} - J_{nl}) \propto P_{out}$, i.e., the threshold current J_{th} approximates the nonlasing current J_{nl} (the current that will be measured on nonlasing device). Consequently, the fit of the current dynamic range can be affected by underestimation of the electron excess temperature because the electron temperature may increase at the nonlasing maximum current biasing conditions with respect to the threshold biasing conditions [21–23].

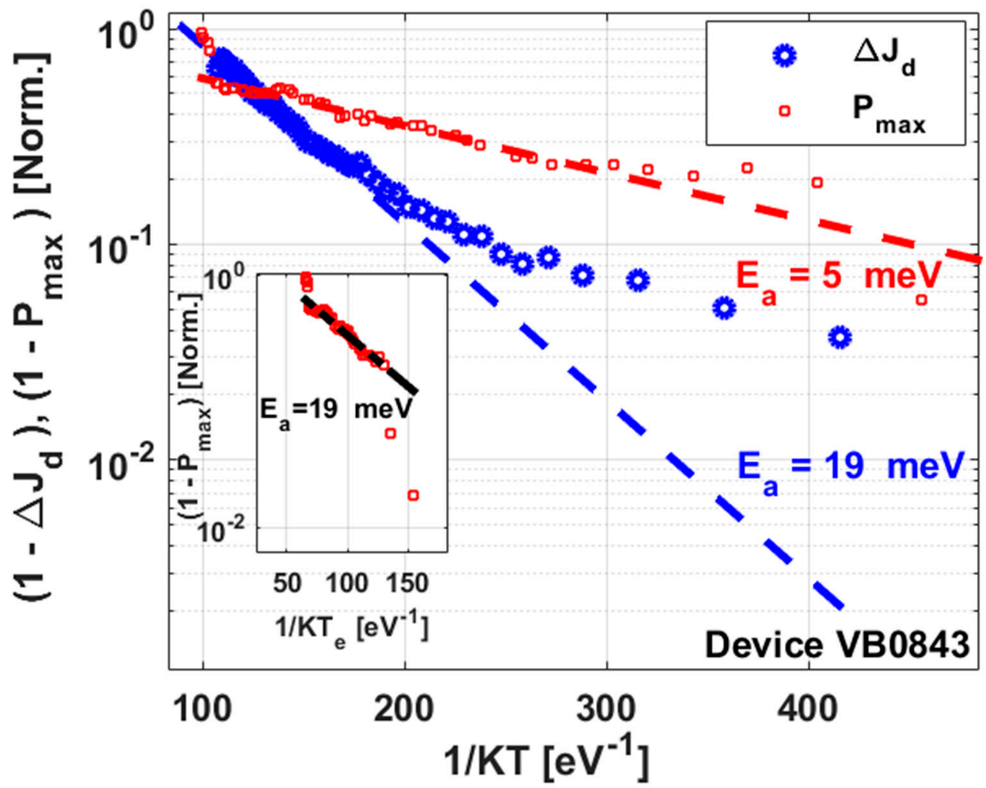

Figure 4. Activation energy extracted from the current dynamic range $\Delta J_d = (J_{max} - J_{th})$ (blue circles) and the laser's maximum power output (P_{max}) (red squares), for Device 1 (wafer VB0843). The quantities in the y-axis are $\left(1 - \frac{\Delta J_d(T)}{\Delta J_{d\,max}}\right)$ and $\left(1 - \frac{P_{out}(T)}{P_{out\,max}}\right)$ respectively presented in logarithmic scale. Including a characteristic excess temperature of 60 K in an Arrhenius plot presentation as a function of the total electron temperature rather than the lattice one results in an activation barrier of 19 meV for the laser's maximum power output (P_{max}) (red squares) data (inset), similarly to the current dynamic range $\Delta J_d = (J_{max} - J_{th})$ (blue circles) data with zero excess electron temperature at the main figure.

Given the current dynamic range of Device 1, we extracted an experimental activation energy of ~19 meV (see Figure 4), as expected for thermally activated LO-phonon scattering, i.e., $E_{LO} - h\nu$ [2,12]. Thermally activated leakage channels through excited states were effectively suppressed as indicated by this result. A different result was observed from the analysis of the P_{out} data. We extracted a lower activation energy value from P_{out}, i.e., ~5 meV. We attribute the lower slope to the electrons' nonzero excess temperature at the ULL [7]. We observed in former THz-QCL designs that the ULL temperature converges to the lattice temperature at lattice temperatures above ~100 K [2], for which case we probed an activation energy value that corresponds to the ULL to LLL thermally activated LO-phonon scattering. In Device 1 the leakage channels were strongly suppressed also for hot electrons, and electrons have fewer scattering paths to cool down, so they are kept above the lattice temperature and also at temperatures higher than 100 K. The small activation energy that we observed here is not the real physical activation energy because the electrons at the ULL are much hotter than the lattice. Inclusion of a characteristic excess temperature of ~60 K in an Arrhenius plot presented as a function of the total electron temperature rather than the lattice temperature (Figure 4 inset) would result in an activation barrier of ~19 meV, which is similar to that extracted from the current dynamic range data with zero excess electron temperature.

We consider that the lower slope observed for the P_{out} data analysis allows us to probe a characteristic excess electron temperature through a comparison with the slope of the current dynamic range, i.e., a characteristic excess temperature of ~60 K. This excess temperature indicates that the electrons remain hot above 100 K.

From this analysis of Device 1, we obtained an indication for the physical mechanism behind the lasing instability. We identified that in the ULL in Device 1 electrons did not cool down at temperatures above ~100 K due to a reduced capability for hot electrons to leak into scattering paths through excited states. We interpret that inability for hot electrons to relax through leakage to excited states is behind the intense lasing instability in this device. In devices with more tendency for intramodule leakage due to lower radiative barriers such as Device 2 (wafer VB0837 in Albo et al. [8], Tables 1 and 2), hot electrons could relax more easily through leakage paths (as scattering from the ULL to level 7 in Figure 1 in [8]) and the instability was much more moderate. The main reason for the laser instability may be the formation of electric field domains [9,10] in the NDR region in the absence of parallel leakage channels.

The tendency for lasing instability is more pronounced as the barriers of the laser get higher. For example, when the radiative barriers of Device 2 described by Albo et al. [8] with 15% aluminum ($Al_{0.15}Ga_{0.85}As$) are replaced with radiative barriers containing 30% Al ($Al_{0.30}Ga_{0.70}As$) in Device 3 (wafer VB0847) (Figure 5, Tables 1 and 2), T_{max} drops from ~170 to ~57 K (Table 2). The intense lasing instability behavior in Device 3 is indicated by the comparison of the low temperature I–V curves of the two devices (Figure 6a). The lasing instability in Device 3 is indicated by the fluctuation in the I–V curve in Figure 6a following by an early NDR already at low temperatures. Device 2 presents relatively stable lasing up to temperatures close to its T_{max} as indicated by its I–V and L–I curves in [8]. The threshold current in both devices was the same (Table 2, Figure 6b), which indicates that gain broadening or additional loss do not constitute the detrimental effect. The intermediate case between the two devices is that of Device 1, where all of the barriers contain 30% Al ($Al_{0.30}Ga_{0.70}As$). In this case, T_{max} drops only to ~120 K due to the lasing instability. The calculated interface roughness (IFR) contribution to the gain broadening is large and was about the same for all these three devices (Table 2) and cannot explain the deviation in behavior between these devices. Similar to our structures in this work, one of the first reports on THz-QCLs with variable barrier height can be found in [26].

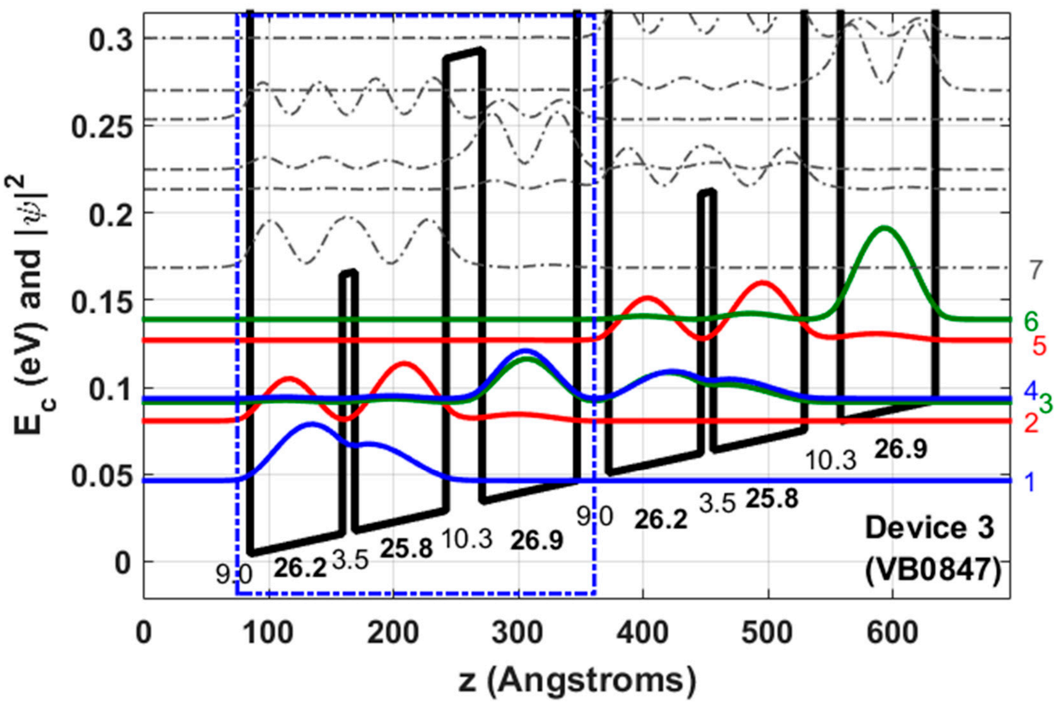

Figure 5. Band diagram of two sequential periods labeled *module i* (left, the dashed-dotted box) and *module i+1* (right) of Device 3 (wafer VB0847) with mixed barriers: the $Al_{0.55}Ga_{0.45}As$ injection barrier, the $Al_{0.30}Ga_{0.70}As$ radiative barrier and the $Al_{0.15}Ga_{0.85}As$ intra-well barrier.

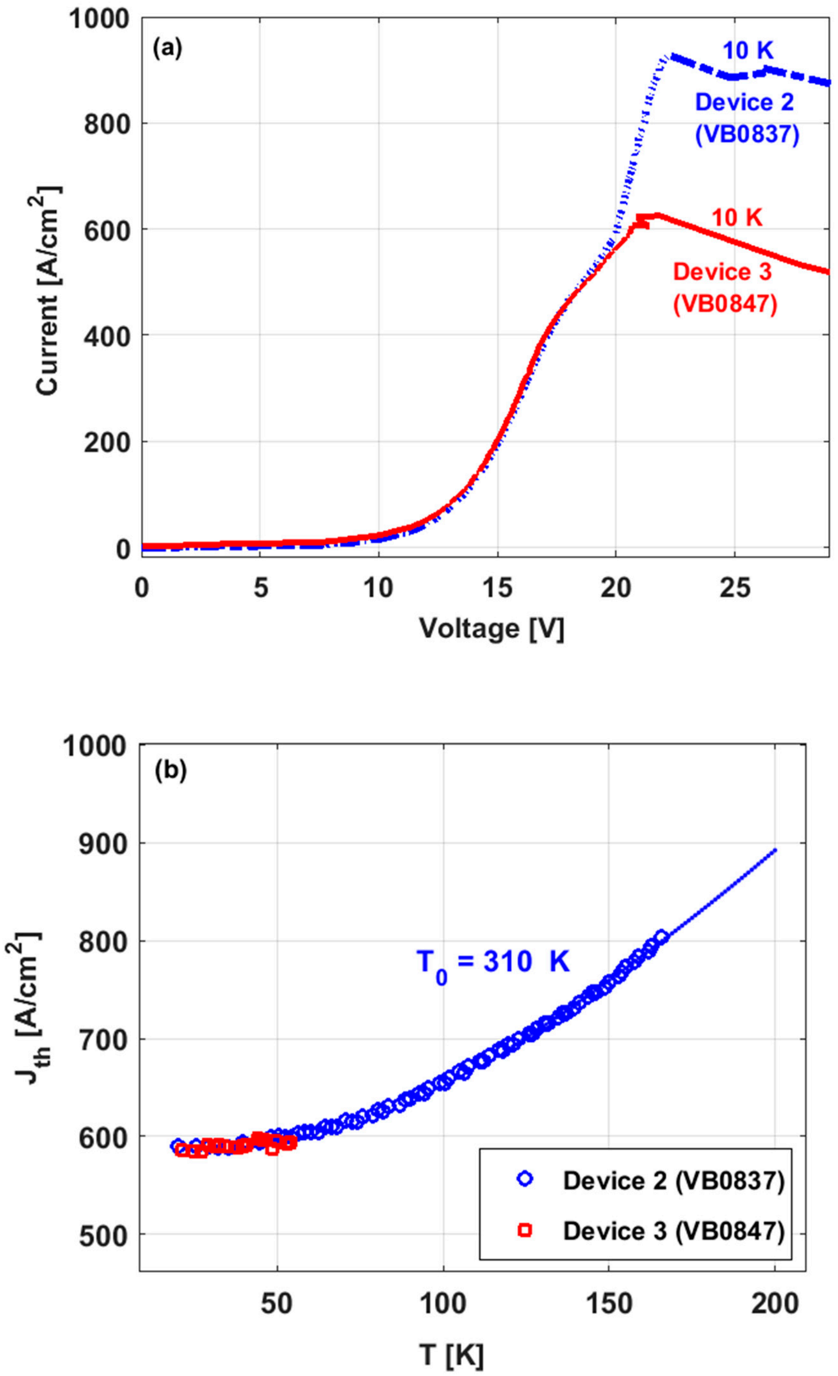

Figure 6. (**a**) Current–voltage curves of Device 3 (VB0847) vs. Device 2 (VB0837) at low temperature. (**b**) Threshold current versus temperature of Devices 3 and 2.

Following observation of the entire experimental data, i.e., of the L–I measurements in Figure 2 and I–V measurements in Figure 3 and their analysis in Figure 4, we consider that the two-slope behavior of the L–I of Device 1 is a characteristic of the increase in excess electron temperature at the ULL as lasing begins, i.e., the second reduced slope of the L–I curves is due to electron heating. The second reduced slope becomes more significant and the L–I curves become flatter as the temperature increases, indicating an increase in electron heat at the ULL as the temperature increases (Figure 2). The second slope eventually disappears (Figure 2), and laser instability begins (Figure 3) and terminates the lasing. The reduced slope and the tendency for lasing instability are both caused by the lack of parasitic leakage from the ULL.

In conclusion, we studied the temperature performance of SWDP THz-QCLs and found that it is limited by lasing instability that becomes significant with increasing temperature. When hot electrons of the ULL cannot leak through scattering to excited states due to the high radiative barriers of the structures, lasing instability occurs and limits the temperature performance. These results indicate that in the SWDP THz-QCLs design, the carrier leakage through excited states must be considered for maintaining stable lasing. More specifically, assuming the temperature performance of Device 2 is limited also by lasing instability, then allowing more leakage from the ULL into the excited state should improve the maximum operating temperature beyond 170 K. For this purpose, the effectiveness of designing thermally-activated IFR leakage paths should be explored.

Funding: This research was funded by the Israel Science Foundation (ISF) grant no. 1556/18.

Acknowledgments: The authors would like to acknowledge the Israel Science Foundation (ISF) for their grant no. 1556/18 and the Bar-Ilan University for their generous Starting Grant for New Faculty Members. The authors also gratefully acknowledge Qing Hu from the Massachusetts Institute of Technology (MIT) for his support in performing this research and further thank John L. Reno from Sandia National Laboratories for the MBE growths.

Conflicts of Interest: The authors declare no conflict of interest.

References

1. Bosco, L.; Franckié, M.; Scalari, G.; Beck, M.; Wacker, A.; Faist, J. Thermoelectrically cooled THz quantum cascade laser operating up to 210 K. *Appl. Phys. Lett.* **2019**, *115*, 010601. [CrossRef]
2. Albo, A.; Hu, Q. Investigating temperature degradation in THz quantum cascade lasers by examination of temperature dependence of output power. *Appl. Phys. Lett.* **2015**, *106*, 131108. [CrossRef]
3. Kumar, S.; Hu, Q.; Reno, J.L. 186 K operation of terahertz quantum-cascade lasers based on a diagonal design. *Appl. Phys. Lett.* **2009**, *94*, 131105. [CrossRef]
4. Albo, A.; Hu, Q. Carrier leakage into the continuum in diagonal GaAs/Al0. 15GaAs terahertz quantum cascade lasers. *Appl. Phys. Lett.* **2015**, *107*, 241101. [CrossRef]
5. Albo, A.; Hu, Q.; Reno, J.L. Room temperature negative differential resistance in terahertz quantum cascade laser structures. *Appl. Phys. Lett.* **2016**, *109*, 081102. [CrossRef]
6. Botez, D.; Kumar, S.; Shin, J.C.; Mawst, L.J.; Vurgaftman, I.; Meyer, J.R. Temperature dependence of the key electro-optical characteristics for midinfrared emitting quantum cascade lasers. *Appl. Phys. Lett.* **2010**, *97*, 071101. [CrossRef]
7. Albo, A.; Flores, Y.V.; Hu, Q.; Reno, J.L. Two-well terahertz quantum cascade lasers with suppressed carrier leakage. *Appl. Phys. Lett.* **2017**, *111*, 111107. [CrossRef]
8. Albo, A.; Flores, Y.V.; Hu, Q.; Reno, J.L. Split-well direct-phonon terahertz quantum cascade lasers. *Appl. Phys. Lett.* **2016**, *114*, 191102. [CrossRef]
9. Winge, D.O.; Dupont, E.; Wacker, A. Ignition of quantum cascade lasers in a state of oscillating electric field domains. *Phys. Rev. A* **2018**, *98*, 023834. [CrossRef]
10. Khabibullin, R.A.; Shchavruk, N.V.; Ponomarev, D.S.; Ushakov, D.V.; Afonenko, A.A.; Maremyanin, K.V.; Volkov, O.Y.; Pavlovskiy, V.V.; Dubinov, A.A. The operation of THz quantum cascade laser in the region of negative differential resistance. *Opto-Electron. Rev.* **2019**, *27*, 329. [CrossRef]
11. Williams, B.S.; Kumar, S.; Qin, Q.; Hu, Q.; Reno, J.L. Terahertz quantum cascade lasers with double-resonant-phonon depopulation. *Appl. Phys. Lett.* **2006**, *88*, 261101. [CrossRef]
12. Kumar, S.; Chan, C.W.I.; Hu, Q.; Reno, J.L. Two-well terahertz quantum-cascade laser with direct intrawell-phonon depopulation. *Appl. Phys. Lett.* **2009**, *95*, 141110. [CrossRef]
13. Scalari, G.; Amanti, M.I.; Walther, C.; Terazzi, R.; Beck, M.; Faist, J. Broadband THz lasing from a photon-phonon quantum cascade structure. *Opt. Express* **2010**, *18*, 8043. [CrossRef] [PubMed]
14. Chan, C.W.I. Towards Room-Temperature Terahertz Quantum Cascade Lasers: Directions and Design. Ph.D. Thesis, Department of Electrical Engineering and Computer Science, Massachusetts Institute of Technology, Cambridge, MA, USA, 2015.
15. Chan, C.W.I.; Albo, A.; Hu, Q.; Reno, J.L. Tradeoffs between oscillator strength and lifetime in terahertz quantum cascade lasers. *Appl. Phys. Lett.* **2016**, *109*, 201104. [CrossRef]

16. Albo, A.; Flores, Y.V. Temperature-driven enhancement of the stimulated emission rate in terahertz quantum cascade lasers. *IEEE J. Quantum Electron.* **2017**, *53*, 2300105. [CrossRef]
17. Franckié, M.; Bosco, L.; Beck, M.; Bonzon, C.; Mavrona, E.; Scalari, G.; Wacker, A.; Faist, J. Two-well quantum cascade laser optimization by non-equilibrium Green's function modelling. *Appl. Phys. Lett.* **2018**, *112*, 021104. [CrossRef]
18. Albo, A.; Flores, Y.V. Carrier leakage dynamics in terahertz quantum cascade lasers. *IEEE J. Quantum Electron.* **2017**, *53*, 8500508. [CrossRef]
19. Baranov, A.N.; Van, H.N.; Loghmari, Z.; Bahriz, M.; Teissier, R. Terahertz quantum cascade laser with non-resonant extraction. *AIP Adv.* **2019**, *9*, 055214. [CrossRef]
20. Franckie, M.; Faist, J. Bayesian Optimization of Terahertz Quantum Cascade Lasers. *Phys. Rev. Appl.* **2020**, *13*, 034025. [CrossRef]
21. Vitiello, M.S.; Scamarcio, G.; Spagnolo, V.; Williams, B.S.; Kumar, S.; Hu, Q.; Reno, J.L. Measurement of subband electronic temperatures and population inversion in THz quantum-cascade lasers. *Appl. Phys. Lett.* **2005**, *86*, 111115. [CrossRef]
22. Harrison, P.; Indjin, D.; Kelsall, R.W. Electron temperature and mechanisms of hot carrier generation in quantum cascade lasers. *J. Appl. Phys.* **2002**, *92*, 6921–6923. [CrossRef]
23. Spagnolo, V.; Scamarcio, G.; Page, H.; Sirtori, C. Simultaneous measurement of the electronic and lattice temperatures in GaAs/Al 0.45 Ga 0.55 as quantum-cascade lasers: Influence on the optical performance. *Appl. Phys. Lett.* **2004**, *84*, 3690–3692. [CrossRef]
24. Almqvist, T.; Winge, D.O.; Dupont, E.; Wacker, A. Domain formation and self-sustained oscillations in quantum cascade lasers. *Eur. Phys. J. B* **2019**, *92*, 72. [CrossRef]
25. Flores, Y.V.; Albo, A. Impact of interface roughness scattering on the performance of GaAs/Al x Ga 1–x as terahertz quantum cascade lasers. *IEEE J. Quantum Electron.* **2017**, *53*, 1–8.
26. Greck, P.; Birner, S.; Huber, B.; Vogl, P. Efficient method for the calculation of dissipative quantum transport in quantum cascade lasers. *Opt. Express* **2015**, *23*, 6587. [CrossRef]